An iterative CT reconstruction algorithm for fast fluid flow imaging

G. Van Eyndhoven*, K.J. Batenburg, D. Kazantsev, V. Van Nieuwenhove, P.D. Lee, K.J. Dobson, and J. Sijbers

Abstract—The study of fluid flow through solid matter by computed tomography (CT) imaging has many applications, ranging from petroleum and aquifer engineering to biomedical, manufacturing and environmental research. To avoid motion artifacts, current experiments are often limited to slow fluid flow dynamics. This severely limits the applicability of the technique.

In this paper, a new iterative CT reconstruction algorithm for improved temporal/spatial resolution in the imaging of fluid flow through solid matter is introduced. The proposed algorithm exploits prior knowledge in two ways. Firstly, the time-varying object is assumed to consist of stationary (the solid matter) and dynamic regions (the fluid flow). Secondly, the attenuation curve of a particular voxel in the dynamic region is modeled by a piecewise constant function over time, which is in accordance with the actual advancing fluid/air boundary.

Quantitative and qualitative results on different simulation experiments and a real neutron tomography dataset show that, in comparison to state-of-the-art algorithms, the proposed algorithm allows reconstruction from substantially fewer projections per rotation without image quality loss. Therefore, temporal resolution can be substantially increased and thus fluid flow experiments with faster dynamics can be performed.

Index Terms—CT, neutron tomography, iterative reconstruction, fluid flow experiments

I. INTRODUCTION

DYNAMIC computed tomography (CT) is a versatile tool for the non-invasive imaging of time-varying objects, as images collected with high temporal frequency allow the visualization of dynamic processes. The CT technique has great potential in fluid flow experiments, where the main goal is to visualize, understand and model the dynamics of the fluid over time. Recent advances in image acquisition speed are now permitting preliminary studies [1]–[3], but current temporal resolutions are insufficient to capture high speed behavior in low viscosity fluids. True high speed dynamic CT of multi-phase flow has potential applications across petroleum and geoscience research [4]–[6], in civil and environmental

engineering [7]–[10], as well as for biomedical and materials science applications.

Conventionally, each time point (also referred to as *time frame*) in a fluid flow experiment is reconstructed independently using projection data that was acquired over a full 180° (or 360°) angular range, typically using classical analytical algorithms such as filtered back-projection (FBP) [11] or algebraic algorithms like the simultaneous iterative reconstruction technique (SIRT) [12]. Afterwards, the reconstructed 4D (3D+t) volume can be processed further for quantification of the fluid flow. The main issue with this conventional approach is that the dynamic process should be slow enough to ensure a nearly stable object during the acquisition of all projections at every time frame. If this assumption is violated, blurring artifacts distort the reconstructed images and further quantification becomes difficult. A straightforward approach to increase the temporal resolution is to reduce the scanning time at each time frame. This can be achieved by lowering either the number of acquired projections per time frame or the exposure time per projection. However, reducing the number of projections typically results in limited data artifacts in the reconstructed images while shortening the exposure time results in a decreased signal-to-noise ratio. This implies a trade-off between spatial and temporal resolution, which ultimately limits current fluid flow experiments to experiments with slow temporal dynamics. This is especially true for neutron tomography, which can image very low concentrations of hydrous fluids but has long projection acquisition times.

In the literature, several approaches for improving the temporal resolution in fluid flow imaging by means of an adapted reconstruction algorithm have already been suggested. Most approaches assume that an a priori high quality reconstruction of the dry stage (i.e., the sample without fluid flow) is available. The simulated projection data of this reconstruction is then subtracted from the measured projection data of the dynamic object, resulting in projection data that corresponds solely to the dynamic component in the reconstruction, i.e., the fluid flow. Myers et al. utilized this approach to iteratively reconstruct the fluid flow, while also enforcing prior knowledge about the porous nature of the material matrix and dynamics of the fluid flow, allowing for faster fluid flow imaging [13]–[15]. Another way of exploiting the prior image consists of minimizing a sparsity measure on the image difference between the dynamic reconstruction and the prior image. Chen et al. combined this sparsity constraint with a data fidelity term to achieve improved image quality [16]. A more statistical approach, i.e., a maximum a posteriori probability (MAP) estimation method, was presented in [17]. Other approaches

* G. Van Eyndhoven is with the iMinds-Vision Lab, University of Antwerp, B-2610 Wilrijk, Belgium (email: geert.vaneyndhoven@uantwerpen.be).

K. J. Batenburg is with Centrum Wiskunde & Informatica, NL-1090 GB Amsterdam, The Netherlands. He is also with the iMinds-Vision Lab, University of Antwerp, B-2610 Wilrijk, Belgium and Mathematical Institute, Leiden University, NL-2300 RA Leiden, the Netherlands.

D. Kazantsev and P.D. Lee are with the Manchester X-ray Imaging Facility, School of Materials, The University of Manchester, Manchester, M13 9PL, UK and with Research Complex at Harwell, Didcot, Oxfordshire, OX11 0FA, UK.

K.J. Dobson is with the Department of Earth and Environmental Sciences, Ludwig Maximilian University, Thereisenstrasse 41, Munich, 80333, Germany.

J. Sijbers and V. Van Nieuwenhove are with the iMinds-Vision Lab, University of Antwerp, B-2610 Wilrijk, Belgium.

do not rely on a prior high quality image, such as the spatial-temporal regularization approach based on non-local means proposed by Kazantsev et al. [18], [19] and the region-based SIRT (rSIRT) method, which assumes only prior knowledge about the location of stationary voxels and dynamic voxels [20].

In this paper, we present a 4D reconstruction algorithm for fluid flow imaging in which specific models describing the space-time evolution of each voxel are exploited during the reconstruction process. It allows for a substantial reduction of acquired projection data per time frame (thus increasing temporal resolution) while maintaining image quality. The proposed algorithm exploits two types of prior knowledge. Firstly, following the approach of [20], a dynamic reconstruction is generated assuming the presence of stationary regions (the solid matter) and dynamic regions (the fluid flow) throughout the reconstruction domain. Secondly, corresponding to the actual physical advancing fluid/air boundary, the attenuation of a particular voxel over time in the dynamic region can typically be described by a piecewise constant (PWC) function. As such, the attenuation curves of all voxels in the dynamic region are approximated by PWC functions at intermediate iterations.

In Section II, a brief introduction to algebraic reconstruction methods and computed tomography of static and dynamic objects is given. In section III, the region-based SIRT algorithm with intermediate PWC function estimation (rSIRT-PWC) algorithm is introduced. Experiments with simulation phantoms and with a real neutron tomography dataset are reported in Section IV. The results are discussed in Section V and the paper is concluded in Section VI.

II. NOTATION AND CONCEPTS

In this section, the basic notations and concepts of computed tomography are introduced. A brief introduction of the tomography model is given in section II-A. Next, a description of the SIRT algorithm is given in section II-B. Finally, in section II-C, the concepts of computed tomography are generalized from static objects to dynamic objects.

A. Tomography model

In what follows, the tomography model is introduced for the 2D case; extension to 3D, however, is trivial. The reconstructed image of the scanned object is represented on a pixel grid consisting of N pixels. The pixel values of the image are ordered in a column vector $\boldsymbol{x} = (x_j) \in \mathbb{R}^N$. Let M denote the total number of measured projection values for all angles, which are log-corrected and ordered in a vector $\boldsymbol{p} = (p_i) \in \mathbb{R}^M$. We refer to $\boldsymbol{p}$ as the measured *projection data*.

The projection data corresponding to a reconstructed image $\boldsymbol{x}$ can be simulated by forward projecting $\boldsymbol{x}$, resulting in the vector $\boldsymbol{q} = (q_i) \in \mathbb{R}^M$ of which the ith component is defined by the linear combination $q_i := \sum_{j=1}^N w_{ij} x_j$. The weight w_{ij} represents the contribution of pixel j to the projection value with index i, as is illustrated in Fig. 1.

The collection of weights form a sparse matrix $\boldsymbol{W} = (w_{ij}) \in \mathbb{R}^{M \times N}$ that models the relationship between the reconstruction $\boldsymbol{x}$ and the simulated projection data as $\boldsymbol{q} = \boldsymbol{W}\boldsymbol{x}$.
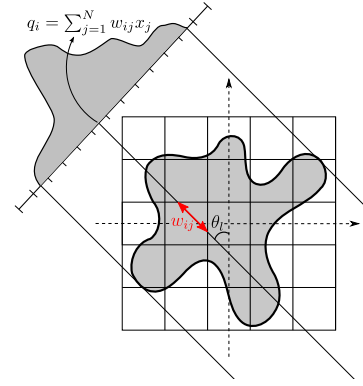

Fig. 1. Illustration of the projection process, with the contribution w_{ij} of pixel j to the projection value with index i represented as the ray-intersection length of projection line i with pixel j.

Directly solving the system of linear equations $\boldsymbol{W}\boldsymbol{x} = \boldsymbol{p}$ for an exact solution $\boldsymbol{x}$ is typically infeasible, since noise and discretization effects render the system of linear equations inconsistent. Therefore, algebraic methods typically minimize the *projection distance* $||\boldsymbol{W}\boldsymbol{x} - \boldsymbol{p}||$ with respect to $\boldsymbol{x}$ for some norm $|| \cdot ||$.

B. SIRT

The methods introduced in this paper are based on the Simultaneous Iterative Reconstruction Technique (SIRT) [12]. SIRT is known to converge to a solution of $\operatorname{argmin}_{\boldsymbol{x}} \left(||\boldsymbol{W}\boldsymbol{x} - \boldsymbol{p}||_{\boldsymbol{R}}^2 \right)$, where $\boldsymbol{R} = (r_{ij}) \in \mathbb{R}^{M \times M}$ is the diagonal matrix with inverse row sums of the projection matrix $\boldsymbol{W}$; its diagonal elements are given by $r_{ii} = 1/\sum_j w_{ij}$. Starting from an initial reconstruction $\boldsymbol{x}^{(0)} = \boldsymbol{0}$, the SIRT algorithm iteratively updates the reconstruction as follows:

$$\boldsymbol{x}^{(k+1)} = \boldsymbol{x}^{(k)} + \boldsymbol{C}\boldsymbol{W}^T \boldsymbol{R}(\boldsymbol{p} - \boldsymbol{W}\boldsymbol{x}^{(k)}) , \qquad (1)$$

where $\boldsymbol{C} = (c_{ij}) \in \mathbb{R}^{N \times N}$ is defined as the diagonal matrix with the inverse column sums of $\boldsymbol{W}$ (i.e., $c_{jj} = 1/\sum_i w_{ij}$).

C. Dynamic set-up

In section II-A, the classical tomography model was described, which assumes the scanned object to remain unaltered throughout the entire data acquisition process. This assumption is no longer valid in fluid flow imaging. Therefore, the dynamic object is typically represented as a time series of images $\boldsymbol{x}_r \in \mathbb{R}^N$, where each $r \in \{1, \ldots, R\}$ is the index referring to a particular point in time (i.e., a *time frame*) and R is the total number of time frames. The entire time series is represented by the vertical concatenation of $\boldsymbol{x}_1, \boldsymbol{x}_2, \ldots, \boldsymbol{x}_R$, i.e., $\tilde{\boldsymbol{x}} := (\boldsymbol{x}_1^T, \boldsymbol{x}_2^T, \ldots, \boldsymbol{x}_R^T)^T \in \mathbb{R}^{RN}$. To reconstruct this time series of images, projection data is acquired for each time frame by rotating source and detector multiple times around the object, or, equivalently, by rotating the object itself in between a fixed source and detector. Standard approaches then typically reconstruct the object at each time frame individually solely based on the projection data corresponding to a single $180°$ or $360°$ rotation.

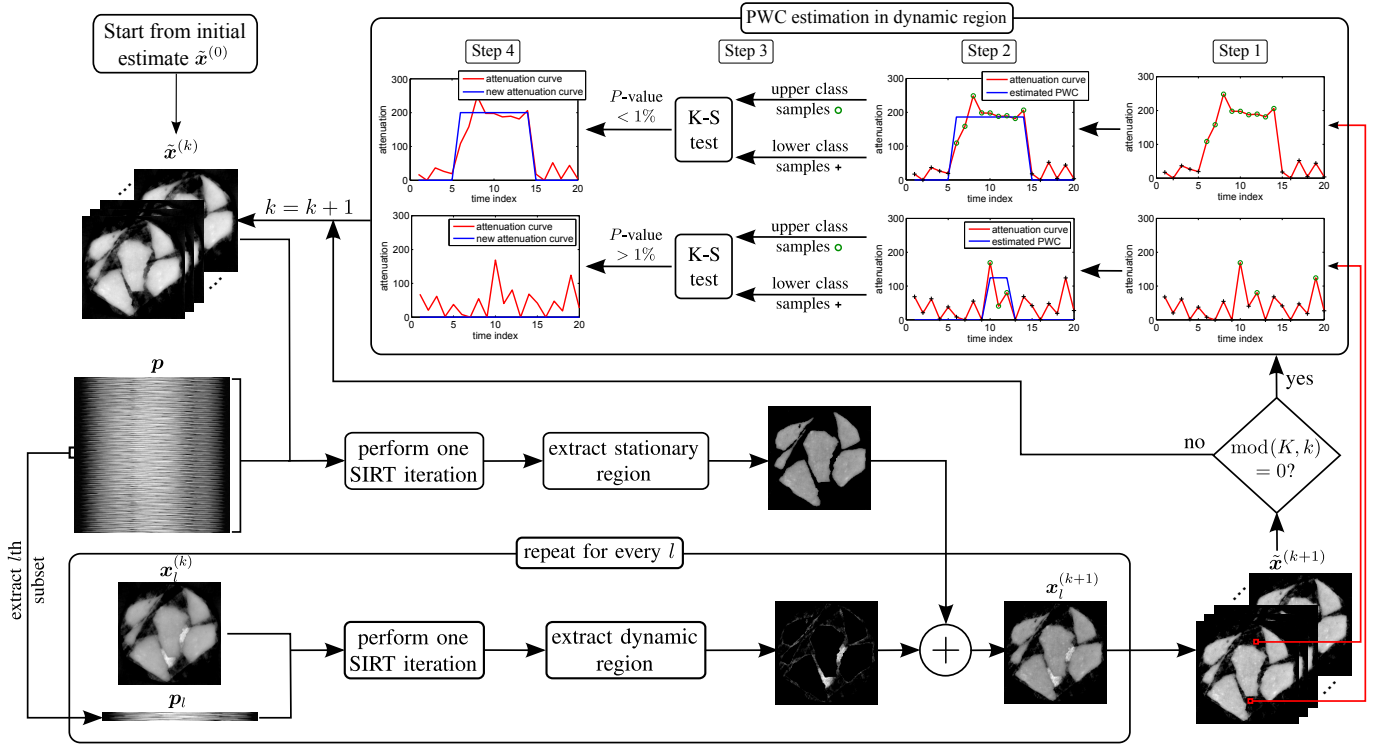There are two main angle selection schemes for acquiring this projection data per time frame:

Fig. 2. Flowchart of the rSIRT-PWC algorithm.

1) A predefined number of equiangular acquisition angles over the complete angular range are defined for each time frame.

2) A "golden ratio" scanning scheme, where source and detector are rotated over a fixed angular step of $\triangle\theta = \pi(1 + \sqrt{5})/2$ radians to determine the next acquisition angle [21].

In the first angle selection scheme the user must select the number of projections per time frame before the experiment starts. The golden ratio scanning scheme is more flexible in the sense that it allows the user to select an arbitrary number of projections per time frame after the data acquisition, while still approximately covering equiangular positions over the entire angular range for each time frame. Since this allows the user to balance the temporal and spatial resolution a posteriori, this scanning protocol was utilized in the experiments of this paper.

For every $r \in \{1, \ldots, R\}$, let $\boldsymbol{p}_r \in \mathbb{R}^M$ be the measured projection data corresponding to the rth time frame. Define $\boldsymbol{W} \in \mathbb{R}^{RM \times N}$ as the forward projection matrix that models all projection angles of the golden ratio scanning scheme and $\boldsymbol{W}_r \in \mathbb{R}^{M \times N}$ as the submatrix of $\boldsymbol{W}$ that models the forward projection for the rth time frame. Furthermore, let the full vector of measured projection data $\tilde{\boldsymbol{p}} \in \mathbb{R}^{RM}$ be the vertical concatenation of $\boldsymbol{p}_1, \boldsymbol{p}_2, \ldots, \boldsymbol{p}_R$. Analogously to the reconstruction problem for the static case, the goal in dynamic tomography is to find a reconstruction $\tilde{\boldsymbol{x}}$ that minimizes

$$||\tilde{\boldsymbol{W}}\tilde{\boldsymbol{x}} - \tilde{\boldsymbol{p}}|| \qquad (2)$$

for some norm $|| \cdot ||$, where $\tilde{\boldsymbol{W}}$ represents the block diagonal matrix consisting of blocks $\boldsymbol{W}_1, \boldsymbol{W}_2, \ldots, \boldsymbol{W}_R$. If only few projections are available per time frame, finding $\tilde{\boldsymbol{x}}$ such that

Eq. (2) is minimal represents an ill-posed problem. This is mainly due to the large null space of the forward operator $\tilde{\boldsymbol{W}}$ and the noise in the measured projection data $\tilde{\boldsymbol{p}}$. This problem can be alleviated by imposing constraints on the reconstruction $\tilde{\boldsymbol{x}}$, resulting in a smaller solution space. Our proposed reconstruction algorithm follows this approach. The enforced model assumptions on the reconstruction $\tilde{\boldsymbol{x}}$ result in a more accurately modeled reconstruction problem, which ultimately leads to better reconstruction quality. Details on the model assumptions are described in the Section III-A.

III. METHOD

The proposed rSIRT-PWC method is visualized in the flowchart of Fig. 2. It is designed to frequently exploit two important model assumptions for fluid flow imaging, which are explained in Section III-A. Starting from an initial estimate $\tilde{\boldsymbol{x}}^{(0)} = \boldsymbol{0}$, rSIRT-PWC continues with the following steps:

1) First, K rSIRT iterations are executed, which is visualized in the bottom most part of the flowchart in Fig. 2.

2) Next, PWC functions are estimated for all voxels in the dynamic region. This is illustrated in the upper most part of the flowchart in Fig. 2.

3) Go back to step 1.

This process is repeated iteratively for K_{tot} iterations. The first step, i.e., the rSIRT iterations, is based on the first model assumption of Section III-A and is explained more thoroughly in Section III-B. The second step in which the PWC functions are estimated is based on the second model assumption of Section III-A and is elaborated in Section III-C.

A. Model assumptions

In fluid flow experiments, several assumptions about the scanned object can be made:

1) The presence of stationary regions: The scanned object is assumed to consist of stationary regions (the solid matter) and regions that change over time, i.e., dynamic regions (the fluid flow). In mathematical terms, this assumption means that there is a set $S \subset \{1, \ldots, N\}$ of voxel indices that correspond to the stationary regions, such that $\boldsymbol{x}_r(j) = \boldsymbol{x}_{r'}(j)$ for all $j \in S$ and $r, r' \in \{1, \ldots, R\}$. This is not necessarily true for voxels in the dynamic region, of which the voxel indices belong to $V := \{1, \ldots, N\} \backslash S$. These sets ($S$ and V) can be calculated prior to the actual fluid flow experiment by generating a segmentation of the solid matter based on a reconstruction of the object before the fluid flow initiated.

In what follows, the set V is further partitioned into two distinct subsets $V = V_B \cup V_F$ with $V_B \cap V_F = \emptyset$. The set V_B contains the indices corresponding to voxels on the border between the dynamic and the stationary region and the set $V_F = V \backslash V_B$ contains indices corresponding to voxels that are fully inside the dynamic region.

2) Two-phase incompressible fluid flow: Since a two-phase incompressible fluid flow is imaged, voxels in the dynamic region can only contain fluid or air. Furthermore, the attenuation value of a homogeneous incompressible fluid is a fixed value (in space and time). This means that, in the dynamic region, the attenuation over time of a particular voxel, i.e., its *attenuation curve*, can be modeled by a PWC function with one fixed attenuation value for the fluid and a zero attenuation value for air, in full accordance with the actual physically advancing fluid/air boundary. That is, in the first time frame, a voxel will contain air. At a certain point in time, fluid will enter the voxel and the voxel's attenuation value will change to the attenuation value of the fluid. Once the fluid leaves the voxel, the attenuation value will return to zero. This can be modeled by a PWC function. In what follows, the attenuation value of the fluid is denoted as a_f.

B. region-based SIRT (rSIRT)

Let $\boldsymbol{I}_V \in \{0, 1\}^{N \times N}$ be the binary diagonal matrix representing the operator that sets all voxels belonging to the stationary region to 0. Its diagonal elements are given by $\boldsymbol{I}_V(j, j) = \chi_V(j)$ where χ_V is the characteristic function for the set V. Analogously, the binary diagonal matrix $\boldsymbol{I}_S \in \{0, 1\}^{N \times N}$ is defined as the operator setting all voxels in the dynamic region to 0, i.e., $\boldsymbol{I}_S(j, j) = \chi_S(j)$. Finally, define $\boldsymbol{R}_r \in \mathbb{R}^{M \times M}$ and $\boldsymbol{C}_r \in \mathbb{R}^{N \times N}$ as the diagonal matrices with inverse row sums and inverse column sums of $\boldsymbol{W}_r$, respectively. The introduced notations allow us to describe the rSIRT algorithm as the following iterative process:

$$\begin{aligned} \boldsymbol{x}_r^{(k+1)} = \boldsymbol{x}_r^{(k)} \ &+ \ \boldsymbol{I}_S \boldsymbol{C} \boldsymbol{W}^T \boldsymbol{R} (\tilde{\boldsymbol{p}} - \tilde{\boldsymbol{W}} \tilde{\boldsymbol{x}}^{(k)}) \\ &+ \ \boldsymbol{I}_V \boldsymbol{C}_r \boldsymbol{W}_r^T \boldsymbol{R}_r (\boldsymbol{p}_r - \boldsymbol{W}_r \boldsymbol{x}_r^{(k)}). \end{aligned} \quad (3)$$

This update needs to be calculated for every $r \in \{1, \ldots, R\}$ before incrementing the iteration count k. Eq. (3) calculates a traditional SIRT update for the stationary region using all available projection data $\tilde{\boldsymbol{p}}$ and then a second update for

the dynamic region using only the projection data from the relevant time frame.

C. Piecewise constant function estimation

In the dynamic region, the attenuation curves of each voxel are replaced by PWC functions at intermediate iterations. The PWC functions are estimated with a different approach depending on the position of the specific voxel. The different types of distinguished voxel positions are displayed in Fig. 3.
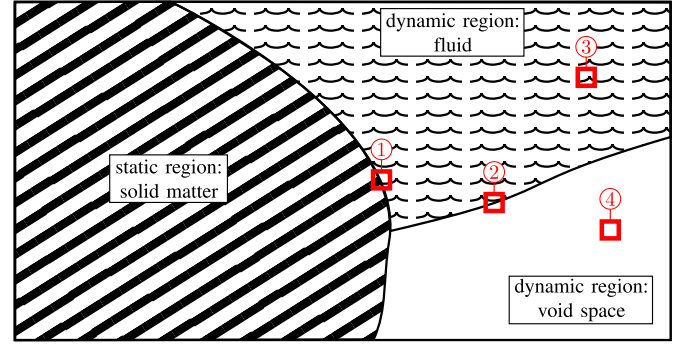

Fig. 3. Illustration of the different types of voxels. Voxel type #1 is situated on the border between the dynamic and the stationary region. Voxels of type #3 are in the fully dynamic region and contain fluid at some point in time. Voxels of type #4 are also classified as dynamic but never contain fluid. Voxel type #2 is located on the border of the fluid and void space in the fully dynamic region.

The set V_B corresponds to voxels of type #1. The voxel types in the fully dynamic region V_F, i.e., voxel types #2, #3 and #4, are assigned during each PWC estimation step, which is explained below.

1) Voxels in the fully dynamic region V_F: The PWC estimation for voxels in the fully dynamic region V_F is subdivided into 4 steps (upper panel in Fig. 2).

In the *first step*, the time attenuation curve (TAC) is extracted for each voxel with index $j \in V_F$. It is defined by $TAC_j(t_r) = \boldsymbol{x}_r(j)$, where t_r represents the time corresponding to the rth time frame. For each of these attenuation curves, a two-class Otsu segmentation [22] of the attenuation values is calculated.

In the *second step*, the mean of the attenuation values in the upper Otsu class, defined as M_j, is utilized to define the PWC function

$$PWC_{t_a, t_b}^{0, M_j}(t) = \begin{cases} M_j & \text{if } t_a < t < t_b \\ 0 & \text{otherwise} \end{cases}, \quad (4)$$

where t_a and t_b are discrete parameters that can be chosen from the finite set $\{t_1, \ldots, t_R\}$, indicating the time points at which the fluid enters and exits the voxel. Note that the PWC function was defined with the mean M_j of the upper Otsu segmentation class rather than the fluid's attenuation value a_f, because iterative algorithms like SIRT typically underestimate the higher attenuation values in the first iterations. This function is used to approximate the extracted attenuation curves TAC_j by solving the following problem:

$$(t_a, t_b) = \underset{t_a, t_b}{\operatorname{argmin}} \sum_{r=1}^{R} (PWC_{t_a, t_b}^{0, M_j}(t_r) - TAC_j(t_r))^2 \ . \quad (5)$$

Eq. (5) is solved by testing all possible combinations of t_a and t_b.

In the *third step*, a statistical test is performed to check whether or not the estimated PWC is relevant. For this purpose, the attenuation values in the original attenuation curve for which $t_a < t < t_b$ (referred to as upper class samples) and for which $(t < t_a)|(t > t_b)$ (referred to as lower class samples) are extracted. With these two sets of samples, a Kolmogorov-Smirnov (K-S) test is performed, which checks the nul hypothesis that claims that the upper and lower class samples are drawn from the same underlying continuous population [23]. This nul hypothesis is rejected at a significance level of 1%, i.e., if the associated P-value is less than 1%. With a rejection of the nul hypothesis, the two sets of samples (the upper and the lower class) are regarded as sufficiently separated and hence the estimated PWC is regarded as relevant, i.e., it does not fit the noise in the extracted attenuation curve.

In the *fourth step*, the attenuation curves are replaced by different PWC functions depending on the type of voxel (type #2, #3 or #4). To obtain the type of each voxel, the fully dynamic region V_F is subdivided using two conditions that determine if a voxel contains fluid over time:

1) The K-S test, performed in step 3, results in a rejection of the nul hypothesis at a 1% significance level. This indicates that the different classes are sufficiently separated.
2) The upper class mean attenuation value (i.e., the mean of TAC_j for time points satisfying $t_a < t < t_b$) is larger than $a_f/2$.

The region of voxels that contain fluid over time is defined by voxels that satisfy both conditions. Voxels on the border of this region are assigned type #2 and voxels that are fully contained in this region (i.e., not on the border) are assigned type #3. If the nul hypothesis is not rejected at the 1% significance level or the mean of the upper class is smaller than $a_f/2$, the voxel is assigned type #4.

Since voxels of type #2 contain both fluid and air, their attenuation curve is replaced by the PWC curve defined in Eq. (4). Voxels of type #3 are either fully emersed by fluid or contain only void space, therefore their corresponding attenuation curves are replaced by

$$PWC_{t_a,t_b}^{0,a_f}(t) = \left\{ \begin{array}{ll} a_f & \text{if } t_a < t < t_b \\ 0 & \text{otherwise} \end{array} \right. . \qquad (6)$$

Voxels of type #4 never contain any fluid and are hence replaced by zero.

2) Voxels in the stationary/dynamic region V_B: The four steps of the PWC estimation procedure introduced previously are slightly adjusted. Since voxels in the stationary/dynamic region V_B can contain a combination of solid matter and fluid or air, the use of a PWC function as defined in Eq. (4) is incorrect. Instead, the mean of the lower Otsu class m_j is calculated in step 1 and the attenuation curves are approximated by the PWC function

$$PWC_{t_a,t_b}^{m_j,M_j}(t) = \left\{ \begin{array}{ll} M_j & \text{if } t_a < t < t_b \\ m_j & \text{otherwise} \end{array} \right. \qquad (7)$$

in step 2. The same K-S test is performed in step 3. Finally, in step 4, the attenuation curves are replaced by Eq. (7) if the null hypothesis is rejected at the 1% significance level and by their mean if the null hypothesis is accepted.

IV. Experiments

In this section, various experiments for the validation of the rSIRT-PWC algorithm are described. First, the figures of merit are introduced in Section IV-A and the reconstruction methods to which rSIRT-PWC is compared are described in Section IV-B. Next, in Section IV-C, different simulation experiments are introduced. An experiment with real neutron tomography data is described in Section IV-D. The results for all these experiments are reported in Section V.

A. Figures of merit

The Relative Root Mean Squared Error (RRMSE) is utilized as a quality measure and is defined as

$$RRMSE(\tilde{x}) = \sqrt{\frac{\sum_i (\tilde{x}(i) - \tilde{y}(i))^2}{\sum_i (\tilde{y}(i))^2}} , \qquad (8)$$

where $\tilde{x}$ denotes the calculated reconstruction and $\tilde{y}$ denotes the ground truth phantom. For some experiments, the RRMSE is inspected only in a Region of Interest (ROI), in which case the sum in Eq. (8) sums over all points in time and over all voxels in the specific ROI.

B. Reconstruction methods

The rSIRT-PWC method is compared to the following reconstruction methods.

- *SIRT*: The SIRT algorithm (see Section II-B) individually applied to the projection data associated with each time frame.
- *SIRT PWC*: In order to have a fair comparison, the SIRT reconstruction was also post-processed with our PWC function estimation method. We refer to this reconstruction as SIRT PWC.
- *rSIRT*: The region-based SIRT algorithm (see Section III-B and [20]).
- *Myers et al.*: The fluid flow reconstruction method introduced by Myers et al. and implemented as described in [13]. For the numerical experiments, the reconstructions are modeled on a 200×200 voxel grid. Therefore, following Myers et al., the static reconstruction was calculated with FBP based on the full set of $315 \approx 200 * \pi/2$ projections, which guarantees accurate image quality [24]. These projections were simulated from the ground truth image assuming an incoming beam intensity of $I_0 = 5 \times 10^4$ (photon count), which is 10 times the number of photons that were assumed for generating the projections of the dynamically evolving object. Also, the soft thresholding parameter and convergence tolerance (which is denoted by ϵ in [13]) were optimized by selecting those parameters that gave the lowest RRMSE with respect to the ground truth. This optimal parameter selection was repeated for each and every experiment. That is, whenever a different number of projections per

time frame was utilized, new optimal parameters were selected, thereby applying the method by Myers et al. at its full strength. In the neutron tomography experiment, there is no ground truth available. Therefore, the algorithmic parameters were chosen manually by visual assessment for the neutron data. All other parameters were chosen as described in [13].

- *CGLS-NLST*: The Conjugate Gradient Least Squares method with Non-Local Spatio-Temporal penalty (CGLS-NLST) developed by Kazantsev et al. and implemented as described in [19]. The reader is referred to [19] for details about the method and its parameters. The prior image containing structural information was set to be the same static reconstruction that was utilized in the method by Meyers et al. Most algorithm parameters were adapted from [19], except for the number of iterations, the regularization parameter and the noise-dependent parameter (denoted by *MaxOuter*, β and h in [19], respectively), since these parameters are problem dependent. These three parameters were optimized for lowest RRMSE with respect to the ground truth for each and every experiment in the simulation experiments and selected manually based on visual assessment in the neutron tomography experiment. The parameter expressing the level of trust (strength of smoothing) in the dynamic data (denoted by γ in [19]) was also manually tuned in the neutron tomography experiment.

The rSIRT-PWC algorithm was implemented as described in Section III with the PWC estimation applied every 20th iteration starting from the 60th iteration. Every method was implemented with a positivity constraint, i.e., voxels with an attenuation value smaller than zero are set to zero after each iteration. All reconstruction methods were applied with 200 iterations, with the exception of the CGLS-NLST method, where this parameter was optimized for lowest RRMSE with respect to the ground truth image. The algorithms were implemented with the ASTRA toolbox [25]–[27].

C. Numerical simulations

Two different simulation phantoms were created. In the simulation experiments, the projections were generated with a strip kernel [11] and a parallel beam geometry. The data was simulated from a higher resolution version of the phantom, i.e., on a 400×400 isotropic voxel grid. The number of detector bins was set to 200, with each detector pixel of twice the size as the voxel size in the high resolution version of the phantom. Projection angles were selected with the golden ratio scanning scheme. Poisson distributed noise was applied to the projection data, assuming an incoming beam intensity of 5×10^3 (photon count). Reconstructions were calculated on a 200×200 isotropic voxel grid and with a linear projection model [11], to avoid the "inverse crime" of generating the data with the same model as the model for calculating the reconstruction [28].
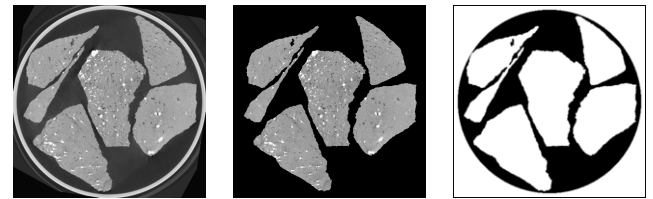
1) Shepp-Logan phantom: The first phantom is a Shepp-Logan type phantom in which fluid flows from one chamber into another during the acquisition of the CT data. The phantom was simulated on 20 time frames, of which frame 1, 10

and 20 are displayed in Fig. 4(a), (b) and (c), respectively. The mask that separates the stationary from the dynamic voxels is displayed in Fig. 4(d). For each time frame, 10 projections were simulated.

(a)   (b)   (c)   (d)

Fig. 4. The adjusted Shepp-Logan phantom on time frame 1, 10 and 20 (a-c) and the mask for stationary region (d), where the white and black region correspond to the stationary and the dynamic region, respectively.

2) Porous rock phantom: The second simulation phantom was created from a high quality FBP reconstruction of an X-ray tomography dataset of rock (porous gravel) acquired on a Nikon XTH 225 ST scanner at the Manchester X-ray Imaging Facility (Fig. 5(a)). In this reconstruction, all voxels

(a) High quality FBP re- (b) Processed FBP re- (c) Mask for the station-
construction   construction   ary region

Fig. 5. The high quality reconstruction of the porous gravel (a), its segmented version (b) and the corresponding mask for the stationary region (c).

that do not belong to the rock (the void volume) were set to zero (Fig. 5(b)) and fluid flow was simulated in the void space. The time point at which the fluid enters a certain voxel was randomly generated by a properly scaled 2D Perlin noise image [29], the same approach was utilized to select the time point at which the fluid leaves a certain voxel. The stationary region (Fig. 5(c)) was defined as the region containing rock and the region outside the sample container. The phantom was simulated on 20 time frames, of which frame 1, 4, 5, 10, 15 and 20 are displayed in the first row of Fig. 9. In this experiment, 20 projections were simulated per time frame.

D. Neutron tomography dataset

A neutron tomography dataset was acquired at the cold neutron imaging Beamline ICON at the SINQ spallation neutron source, Paul Scherrer Institute, Switzerland. Granitic gravel particles with a 5-10 mm diameter were loaded into a 25 mm thin walled Al tube and mounted in a gravity driven flow cell. Parallel beam projection images were acquired under the golden ratio scanning scheme [30] with an exposure time of 20 seconds per projection. After a 2×2 rebinning, the dimension of the detector was given by 1023×1030 pixels with pixel size 26 μm. Reconstructions were calculated on the central slice on a 1030×1030 pixel grid, also with pixel size 26 μm. Initially, the sample was scanned in its dry stage (no fluid flow) at 154 projection angles and a reconstruction was calculated

with 200 SIRT iterations (Fig. 6(a)). A mask for the stationary region (Fig. 6(b)) was extracted from this SIRT reconstruction. Next, after starting the fluid flow, another 326 "wet stage" projections were acquired. The projection data of the dry stage and the wet stage were combined to form a projection data set corresponding to 480 projection angles. This set of projections served as the input for all evaluated reconstruction methods. Since angles were selected with the golden ratio scanning scheme, the projection data can be subdivided in arbitrary subsets which allows for selecting the number of time frames as desired.

The stationary region mask in Fig. 6(b) was utilized as prior knowledge in rSIRT, rSIRT-PWC and the method by Myers et al. The latter method and CGLS-NLST were applied with the dry stage SIRT reconstruction (Fig. 6(a)) as the prior image.
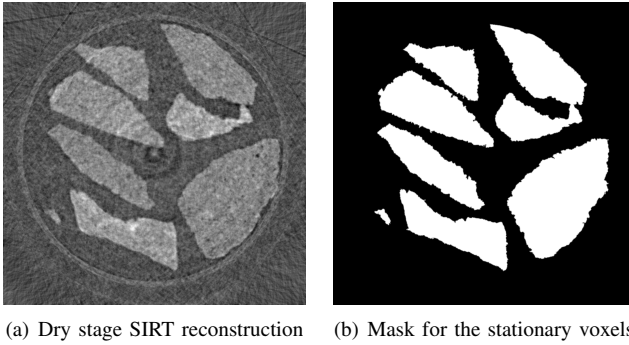

(a) Dry stage SIRT reconstruction   (b) Mask for the stationary voxels

Fig. 6. The dry stage reconstruction (a) and the extracted mask (b) of the gravel particles in the neutron tomography experiment.

V. RESULTS

A. Shepp-Logan phantom

Frame 10 of the reconstructions for all algorithms are displayed in Fig. 7. The reconstruction method by Myers et al. is based on more projection data (i.e., the projection data to generate the prior image and the projection data acquired from the dynamically evolving object) in comparison to the other methods. A fully fair comparison is hence only possible if the rSIRT-PWC method is allowed to use this projection data as well. For this reason, the reconstruction in Fig. 7(g) was created, it is the rSIRT-PWC reconstruction generated from the combination of the projection data used in the generation of the prior image for the method by Myers et al. and the projection data acquired from the dynamically evolving object. From Fig. 7, it is obvious that the standard SIRT algorithm suffers from limited data artifacts. This is improved by rSIRT (Fig. 7(c)) and substantially improved by CGLS-NLST, the method of Myers et al. and rSIRT-PWC (Fig. 7(d-g)). Furthermore, the rSIRT-PWC has better image quality in the dynamic region in comparison to CGLS-NLST and the method by Myers et al. These observations are confirmed by the RRMSE values in Table I. Since the reconstruction by the method of Myers et al. is based on a prior high quality reconstruction, it is obvious that it has better image quality in the stationary region.

To test the algorithms' performance with respect to the amount of available projection data, the previous experiment

	SIRT	SIRT PWC	rSIRT	CGLS-NLST	Myers et al.	rSIRT-PWC
full ROI	0.5938	0.5819	0.2598	0.3806	0.2796	**0.2536**
stat. ROI	0.6414	0.6406	0.2653	0.4117	**0.2607**	0.2669
dyn. ROI	0.3845	0.3014	0.2304	0.2360	0.3187	**0.1905**

TABLE I
RRMSE VALUES FOR THE SHEPP-LOGAN PHANTOM EVALUATED FOR DIFFERENT RECONSTRUCTIONS (COLUMNS) IN THE FULL RECONSTRUCTION DOMAIN (FIRST ROW), IN THE STATIONARY ROI (MIDDLE ROW) AND IN THE DYNAMIC ROI (LAST ROW). IN THIS EXPERIMENT, 10 PROJECTIONS WERE SIMULATED PER TIME FRAME.

was repeated for a varying number of projections per time frame, while keeping all other experimental parameters the same. The RRMSE for each of these experiments is plotted as function of the number of projections per time frame in Fig. 8. From these plots, it is obvious that rSIRT-PWC outperforms all other reconstruction methods in almost all scenarios. One exception is the stationary region's image quality if only few projection data (less than 15 projections per time frame) is available: in this case the method by Myers et al. gives better results than the proposed rSIRT-PWC method. This is again due to the fact that the stationary region's reconstruction for the method by Myers et al. is based on more projection data (315 projections) than the rSIRT-PWC reconstruction. As soon as sufficient projection data becomes available (more than 15 projections per time frame), the rSIRT-PWC method also outperforms the method of Myers et al. with respect to image quality in the stationary region. Furthermore, by comparing the RRMSE values at 50 projections per time frame for the SIRT method and 5 projections per time frame for the rSIRT-PWC method in Fig. 8(c), it can be observed that the rSIRT-PWC reconstruction method achieves comparable image quality in the dynamic region with up to an order of magnitude fewer projections than the conventional SIRT method.

B. Porous rock phantom

The reconstructions in time frame 1, 4, 5, 10, 15 and 20 for all algorithms are displayed in Fig. 9. The RRMSE values can be found in Table II. It is clear, both visually from Fig. 9 and

	SIRT	SIRT PWC	rSIRT	CGLS-NLST	Myers et al.	rSIRT-PWC
full ROI	0.3084	0.2716	0.2037	0.2004	0.1839	**0.1655**
stat. ROI	0.2472	0.2446	0.1488	0.1597	0.1479	**0.1357**
dyn. ROI	0.8999	0.4974	0.6358	0.4984	0.4637	**0.3330**

TABLE II
RRMSE VALUES FOR THE POROUS ROCK PHANTOM EVALUATED IN THE FULL RECONSTRUCTION DOMAIN (FIRST ROW), IN THE STATIONARY ROI (MIDDLE ROW) AND IN THE DYNAMIC ROI (LAST ROW). THE DIFFERENT COLUMNS REPRESENT DIFFERENT RECONSTRUCTION ALGORITHMS. IN THIS EXPERIMENT, 20 PROJECTIONS WERE SIMULATED PER TIME FRAME.

numerically from Table II, that a conventional reconstruction approach such as SIRT suffers from limited data artifacts if only 20 projections are available per time frame. The rSIRT reconstruction can more accurately reconstruct the stationary region. However, mainly because the lack of model restrictions in the dynamic region, the rSIRT reconstruction is strongly influenced by noise in the dynamic region. The CGLS-NLST method improves image quality in both stationary and dynamic

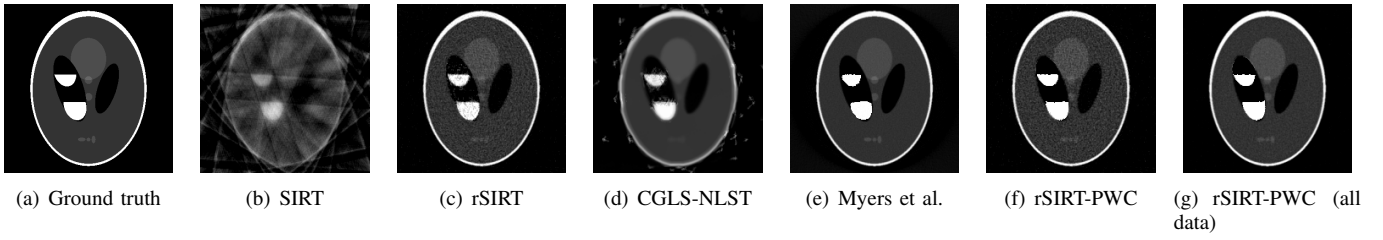| (a) Ground truth | (b) SIRT | (c) rSIRT | (d) CGLS-NLST | (e) Myers et al. | (f) rSIRT-PWC | (g) rSIRT-PWC (all data) |

Fig. 7. Reconstructions (displayed in time frame 10) for the simulation experiment with the adjusted Shepp-Logan phantom. All reconstructions were calculated based on 10 simulated projections per time frame.
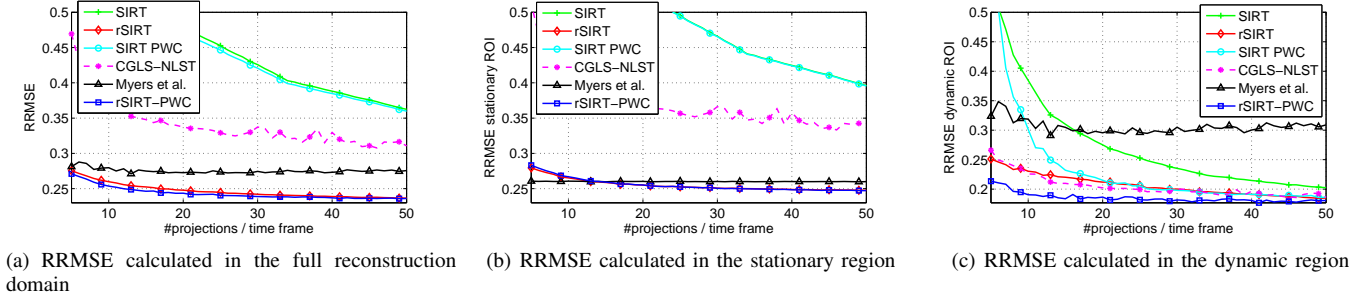

(a) RRMSE calculated in the full reconstruction domain

(b) RRMSE calculated in the stationary region

(c) RRMSE calculated in the dynamic region

Fig. 8. The RRMSE as function of the number of projections per time frame for SIRT, rSIRT, the method by Myers et al. and rSIRT-PWC for the Shepp-Logan phantom.

region, but due to the high level of noise in the projection data and the low number of projections, the optimal smoothing parameters were rather large and hence the fine structures are partially erased. The method by Myers et al. also has improved image quality in both the stationary and the dynamic region. The rSIRT-PWC reconstruction, however, has even better image quality. The fluid's dynamics are captured more correctly and the region on the edge between stationary and dynamic region has a better correspondence to the ground truth image.

The previous experiment was repeated for a varying number of projections per time frame, while keeping all other experimental parameters the same. The RRMSE as function of the number of projections per time frame can be observed in Fig. 10. It can be concluded that the proposed rSIRT-PWC algorithm outperforms all other algorithms. Notice that the stationary region of the reconstruction by Myers et al. has better image quality for a low number of projections per time frame (Fig. 10(b)). This is again due to the fact that this region of the reconstruction domain is based on the prior image, which was reconstructed a priori with FBP based on 315 projection images. The rSIRT-PWC algorithm does not utilize this data. However, starting from around 15 projections per time frame (which corresponds to a total of 300 projections for all 20 time frames) the rSIRT-PWC stationary region reconstruction has better quality than the reconstruction of Myers et al. At that point, rSIRT-PWC has acces to approximately an equal number of projections for reconstructing the stationary region and due to the fact that rSIRT-PWC is based on an iterative technique (which generally outperforms FBP) the reconstruction quality in the stationary region becomes better. Analogously to the Shepp-Logan experiment, it can also be observed in Fig. 10(c) that the rSIRT-PWC reconstruction method achieves comparable

image quality in the dynamic region with up to an order of magnitude fewer projections than the other methods.

C. Neutron tomography dataset

The projection dataset was first subdivided into 48 time frames of 10 projections each. The corresponding reconstructions generated by SIRT, rSIRT, CGLS-NLST, the method by Myers et al. and rSIRT-PWC on time frame 1, 30, 31 and 48 are displayed in Fig. 11. The reconstructions generated by SIRT and rSIRT are heavily influenced by both noise and artifacts in the dynamic region, as are those produced by the CGLS-NLST and Myers et al. method because the prior image does not have perfect quality in this experiment. The rSIRT-PWC reconstruction has good contrast both in the stationary and the dynamic regions.

In a second experiment, the projection dataset was respectively subdivided into 10 subsets of 48 projections each, 20 subsets of 24 projections each, 30 subsets of 16 projections each and 48 subsets of 10 projections each. The resulting reconstructions on the last time frame can be observed in Fig. 12. The rSIRT-PWC reconstruction (bottom row in Fig. 12) is the least affected by having small numbers of projections available per time frame, which illustrates the ability of rSIRT-PWC to increase the temporal resolution without affecting the image quality.

VI. CONCLUSION

Capturing the high speed dynamics of fluid flow by means of CT imaging requires a short acquisition time, which can be achieved by acquiring only few projection images per time frame. However, reconstructing data from undersampled projection data is a difficult problem, and conventional approaches that reconstruct the object independently at different time frames result in images containing limited data artifacts.
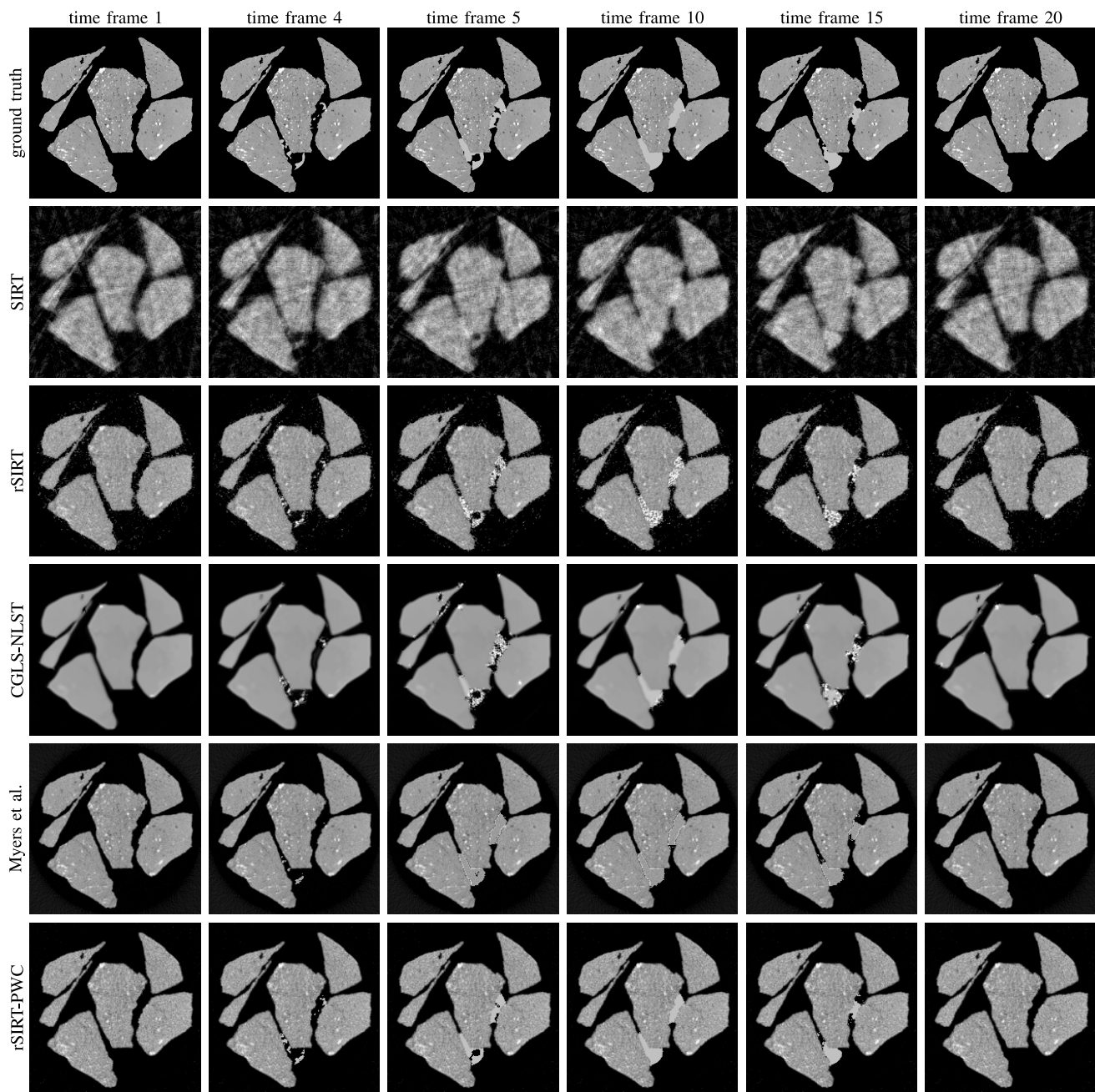
Fig. 9. Ground truth images and reconstructions of the porous rock phantom showing the evolution through time. The columns represent different time frames and the rows represent the ground truth phantom and the different reconstruction methods. All reconstructions are based on 20 simulated projections in each time frame.

In this paper, the rSIRT-PWC algorithm was introduced, an iterative method tailored specifically to fluid flow reconstruction problems. The algorithm divides the reconstruction domain into stationary (the solid matter) and dynamic (the fluid flow) regions, and assumes the shape of the attenuation curves in the dynamic region to be piecewise constant in accordance with a physical advancing air-fluid boundary. Since the reconstruction problem is modeled more accurately, the size of the solution space is substantially reduced and the final image quality improves. Therefore, the rSIRT-PWC algorithm allows for a significant reduction in the number of projections per time frame without image quality loss. The rSIRT-PWC reconstruction method achieves comparable image quality in the dynamic region with up to an order of magnitude fewer projections than conventional methods. It therefore provides a much-needed method for probing high speed fluid dynamics.

ACKNOWLEDGMENT

(a) RRMSE calculated in the full reconstruction domain

(b) RRMSE calculated in the stationary region
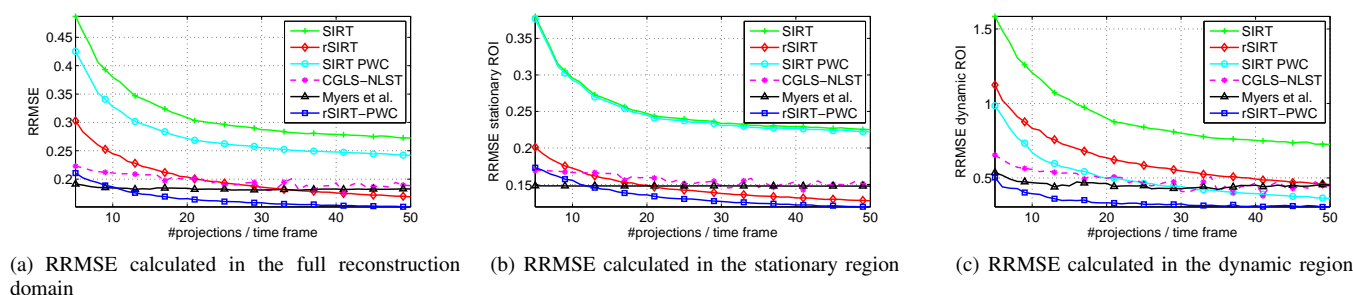
(c) RRMSE calculated in the dynamic region

Fig. 10. The RRMSE as function of the number of projections per time frame for SIRT, rSIRT, the method by Myers et al. and rSIRT-PWC for the porous rock phantom.

REFERENCES

[1] S. Iglauer, A. Paluszny, and M. Blunt, "Corrigendum to simultaneous oil recovery and residual gas storage: A pore-level analysis using in situ x-ray micro-tomography [fuel 103 (2013) 905914]," *Fuel*, vol. 139, no. 0, pp. 780 – 780, 2015.

[2] M. Andrew, B. Bijeljic, and M. J. Blunt, "Pore-by-pore capillary pressure measurements using X-ray microtomography at reservoir conditions: Curvature, snap-off, and remobilization of residual CO_2," *Water. Resour. Res.*, vol. 50, no. 11, pp. 8760–8774, 2014.

[3] ——, "Pore-scale contact angle measurements at reservoir conditions using X-ray microtomography," *Adv. Water Resour.*, vol. 68, no. 0, pp. 24 – 31, 2014.

[4] V. Cnudde and M. Boone, "High-resolution X-ray computed tomography in geosciences: A review of the current technology and applications," *Earth-Sci. Rev.*, vol. 123, pp. 1 – 17, 2013.

[5] R. Dann, M. Turner, M. Close, and M. Knackstedt, "Multi-scale characterisation of coastal sand aquifer media for contaminant transport using X-ray computed tomography," *Environ. Earth Sci.*, vol. 63, no. 5, pp. 1125–1137, 2011.

[6] A. N. Golab, M. A. Knackstedt, H. Averdunk, T. Senden, A. R. Butcher, and P. Jaime, "3D porosity and mineralogy characterization in tight gas sandstones," *Leading Edge*, vol. 29, no. 12, pp. 1476–1483, 2010.

[7] M. Slavíková, F. Krejcí, J. Žemlicka, M. Pech, P. Kotlík, and J. Jakubek, "X-ray radiography and tomography for monitoring the penetration depth of consolidants in Opukathe building stone of Prague monuments," *J. Cult. Herit.*, vol. 13, no. 4, pp. 357 – 364, 2012.

[8] S. Raneri, V. Cnudde, T. De Kock, H. Derluyn, G. Barone, and P. Mazzoleni, "X-ray computed micro-tomography to study the porous structure and degradation processes of a building stone from Sabucina (Sicily)," *Euro. J. of Mineral.*, 2015, to be published.

[9] A. Polak, D. Elsworth, H. Yasuhara, A. S. Grader, and P. M. Halleck, "Permeability reduction of a natural fracture under net dissolution by hydrothermal fluids," *Geophys. Res. Lett.*, vol. 30, no. 20, 2003.

[10] K. Singh, R. K. Niven, T. J. Senden, M. L. Turner, A. P. Sheppard, J. P. Middleton, and M. A. Knackstedt, "Remobilization of residual non-aqueous phase liquid in porous media by freeze-thaw cycles," *Environ. Sci. Technol.*, vol. 45, no. 8, pp. 3473–3478, 2011.

[11] A. C. Kak and M. Slaney, *Principles of Computerized Tomographic Imaging*. SIAM, 2001.

[12] J. Gregor and T. Benson, "Computational analysis and improvement of SIRT," *IEEE Trans. Med. Imag.*, vol. 27, no. 7, pp. 918–24, 2008.

[13] G. R. Myers, A. M. Kingston, T. K. Varslot, M. L. Turner, and A. P. Sheppard, "Dynamic tomography with a priori information," *Appl. Optics*, vol. 50, no. 20, pp. 3685–3690, 2011.

[14] ——, "Dynamic X-ray micro-tomography for real time imaging of drainage and imbibition processes at the pore scale," in *Int. Symp. of the Soc. of Core Analysts, Austin, TX*, 2011, pp. 1–12.

[15] G. Myers, T. Varslot, A. Kingston, A. Herring, and A. Sheppard, "Ground-truth verification of dynamic X-ray micro-tomography images of fluid displacement," in *Proc. SPIE, Developments in X-ray Tomography VIII*, vol. 8506, 2012, p. 85060P.

[16] G.-H. Chen, J. Tang, and S. Leng, "Prior image constrained compressed sensing (PICCS): a method to accurately reconstruct dynamic CT images from highly undersampled projection data sets," *Med. Phys.*, vol. 35, no. 2, pp. 660–663, 2008.

[17] G. R. Myers, M. Geleta, A. M. Kingston, B. Recur, and A. P. Sheppard, "Improving dynamic tomography, through maximum a posteriori estimation," in *Proc. SPIE, Developments in X-Ray Tomography IX*, vol. 9212, 2014, p. 921211.

[18] D. Kazantsev, W. M. Thompson, W. R. B. Lionheart, G. Van Eyndhoven, A. P. Kaestner, K. J. Dobson, P. J. Withers, and P. D. Lee, "4D-CT reconstruction with unified spatial-temporal patch-based regularization," *Inverse Probl. Imag.*, vol. 9, no. 2, pp. 447–467, 2015.

[19] D. Kazantsev, G. Van Eyndhoven, W. R. B. Lionheart, P. J. Withers, K. J. Dobson, S. A. McDonald, R. Atwood, and P. D. Lee, "Employing temporal self-similarity across the entire time domain in computed tomography reconstruction," *Phil. Trans. R. Soc. A*, vol. 373, no. 2043, 2015.

[20] G. Van Eyndhoven, K. J. Batenburg, and J. Sijbers, "Region-based iterative reconstruction of structurally changing objects in CT," *IEEE Trans. Imag. Proc.*, vol. 23, no. 2, pp. 909–919, 2014.

[21] T. Kohler, "A projection access scheme for iterative reconstruction based on the golden section," in *IEEE Nucl. Sci. Conf. R.*, vol. 6, 2004, pp. 3961–3965.

[22] N. Otsu, "A threshold selection method from gray-level histograms," *IEEE Trans. Syst., Man, Cybern.*, vol. 9, no. 1, pp. 62–66, 1979.

[23] F. J. Massey, "The Kolmogorov-Smirnov test for goodness of fit," *J. Am. Stat. Assoc.*, vol. 46, no. 253, pp. 68–78, 1951.

[24] F. Natterer, *The mathematics of computerized tomography*. SIAM, 1986, vol. 32.

[25] W. J. Palenstijn, K. J. Batenburg, and J. Sijbers, "Performance improvements for iterative electron tomography reconstruction using graphics processing units (GPUs)," *J. Struct. Biol.*, vol. 176, no. 2, pp. 250 – 253, 2011.

[26] ——, "The ASTRA tomography toolbox," in *13th Int. Conf. on Comput. and Math. Meth. in Sci. and Eng. CMMSE*, 2013.

[27] W. van Aarle, W. J. Palenstijn, J. De Beenhouwer, T. Altantzis, S. Bals, K. J. Batenburg, and J. Sijbers, "The ASTRA Toolbox: A platform for advanced algorithm development in electron tomography," *Ultramicroscopy*, vol. 157, pp. 35 – 47, 2015.

[28] J. Kaipio and E. Somersalo, "Statistical inverse problems: Discretization, model reduction and inverse crimes," *J. Comput. Appl. Math.*, vol. 198, no. 2, pp. 493–504, 2007.

[29] K. Perlin, "Improving noise," in *ACM T. Graphic.*, vol. 21, no. 3. ACM, 2002, pp. 681–682.

[30] A. Kaestner, B. Munch, T. Pavel, and B. Les, "Spatiotemporal computed tomography of dynamic processes," *Opt. Eng.*, vol. 50, no. 12, p. 123201, 2011.
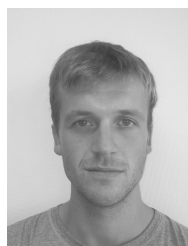
Geert Van Eyndhoven started his studies at the K.U. Leuven, Leuven, Belgium, where he obtained the Bachelor degree in Mathematics and later the M.Sc. degree in Mathematical Engineering, which he received in June 2011. He is currently a Ph.D. student at the iMinds-Vision Lab, Department of Physics, University of Antwerp, Belgium. His doctoral research focusses on iterative reconstruction algorithms in computed tomography, with the main focus on dynamic computed tomography.

This article has been accepted for publication in a future issue of this journal, but has not been fully edited. Content may change prior to final publication. Citation information: DOI 10.1109/TIP.2015.2466113, IEEE Transactions on Image Processing

VAN EYNDHOVEN *et al.*: AN ITERATIVE CT RECONSTRUCTION ALGORITHM FOR FAST FLUID FLOW IMAGING
11

Kees Joost Batenburg received the M.Sc. degree in mathematics and the M.Sc. degree in computer science from the University of Leiden, Leiden, The Netherlands, in 2002 and 2003, respectively, and the Ph.D. degree in mathematics in 2006. He is currently a Senior Researcher at Centrum Wiskunde en Informatica, Amsterdam, where he performs research in the field of computational imaging. He also has two part-time professorships at the University of Antwerp (Belgium) and Leiden (The Netherlands), respectively.

Jan Sijbers received a M.Sc. in Physics in 1993 and a Ph.D. in Sciences/Physics from in 1998 from the University of Antwerp, Belgium. He was a Postdoctoral fellow of the FWO (Fund for Scientific Research) from 2002-2008, jointly at the University of Antwerp and the Delft University of Technology, The Netherlands. Currently, he is a full professor at the University of Antwerp and head of iMinds Vision Lab. His main interest is in biomedical image reconstruction, processing and analysis with focus on diffusion MRI processing and iterative reconstruction for computed tomography.

Daniil Kazantsev completed his PhD in Novosibirsk, Russia in the group of Computerized Tomography in the Institute of Theoretical and Applied Mechanics. As a PDRA he worked in the Center of Medical Imaging Computing (CMIC) at UCL, London, UK. Currently he is a PDRA in the School of Materials, The University of Manchester based at Research Complex at Harwell (MXIF) UK. His main interests are ill-posed inverse problems in transmission and emission tomography, multimodal reconstruction and time lapse tomography.

Vincent Van Nieuwenhove started his studies at the University of Antwerp, Belgium, where he obtained the Bachelor and Master degree in Physics, the latter he received in 2013. Currently he is pursuing a Ph.D. degree at the iMinds-Vision lab, Department of Physics, University of Antwerp, Belgium. His research focusses mainly on dynamic tomography (4DCT) and advanced flat field correction.

Peter D. Lee directs the Diamond-Manchester Collaboration, a joint venture to bring together physicists, biologists, earth and material scientists to develop and apply the next generation of x-ray and multi-modal imaging techniques. The applications focus on investigating the evolution of microstructures using x-ray imaging and computational simulation techniques. Peter has worked in Industry (at Alcan International, 1988-93) and in academia at Imperial College heading the Metallurgy group (1994-2011), and now Manchester. He has an undergraduate degree in Engineering Science, MSc in Metallurgy (University of Toronto), and a D. Phil in Materials Science (Oxford).

Katherine J. Dobson is a volcanologist and geoscientist, and is currently an ERC (EVOKES) supported Postdoctoral Research Fellow at Ludwig-Maximilians Universität, Munich, Germany. She has used strong interdisciplinary skills developed during time in the School of Materials, University of Manchester, UK, to develop a novel geological research program; quantifying dynamic geological processes in 4D using the latest high speed x-ray and neutron tomography techniques.
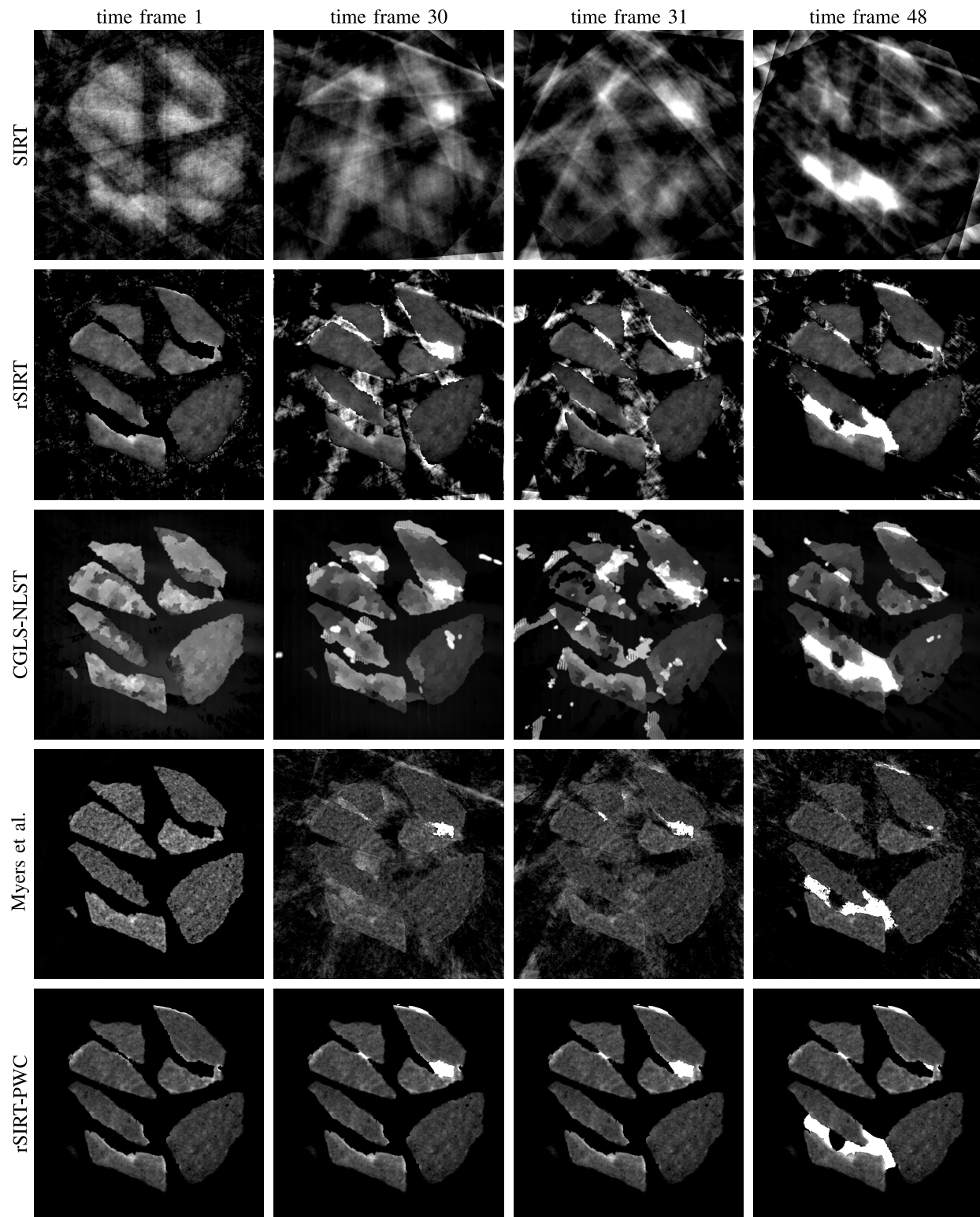
Fig. 11. Single slice through the reconstructed neutron tomography data showing the evolution through time. The columns correspond to different time frames and the rows to the different reconstruction methods. In this experiment, the projection dataset was subdivided in 48 time frames with 10 projections each.
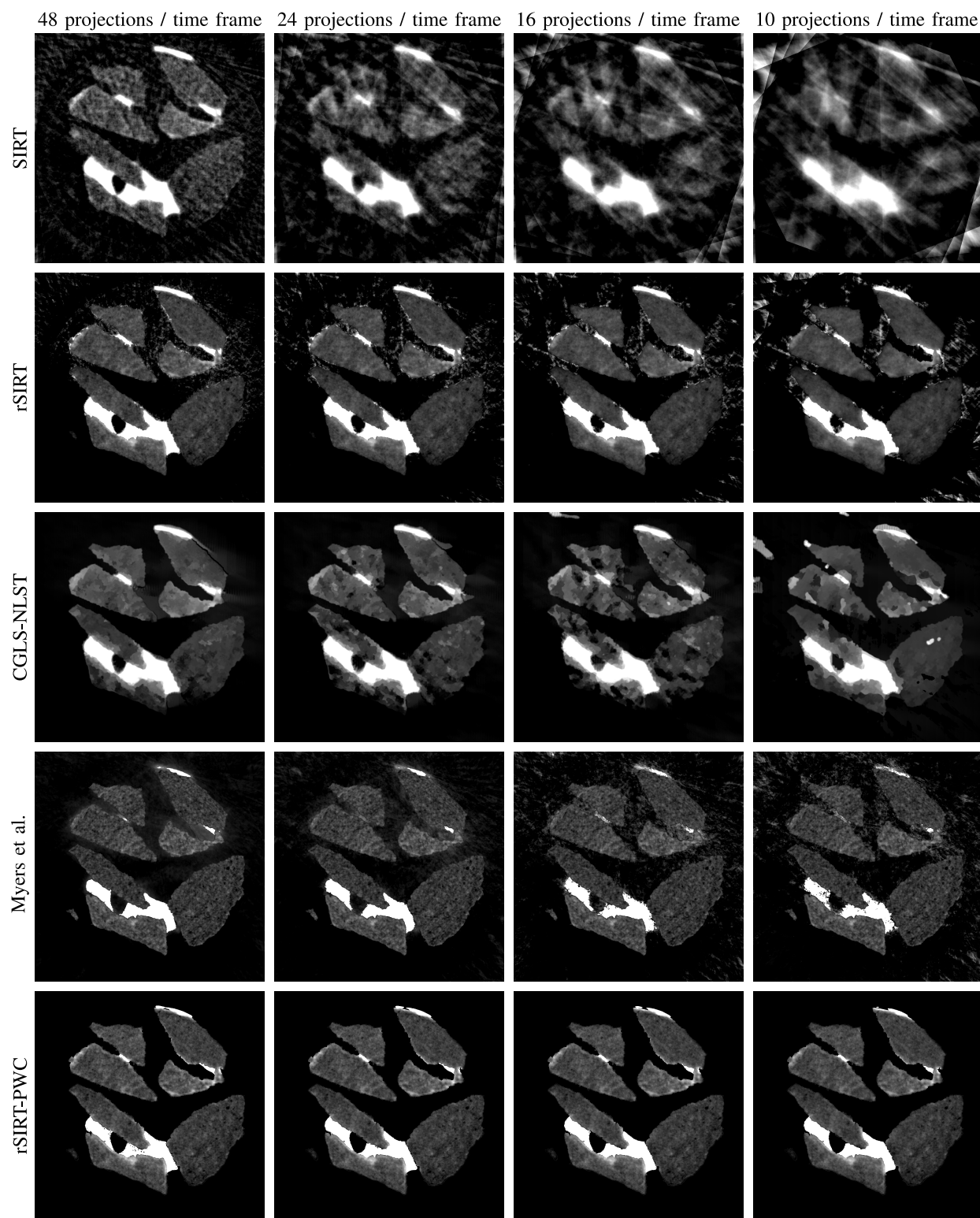
Fig. 12. Single slice through the reconstructed neutron tomography data on the last time frame. Column labels refer to the number of projections per time frame. Row labels indicate the reconstruction method employed.